DRAFT VERSION JUNE 20, 2019
Typeset using LaTeX **twocolumn** style in AASTeX62

Dynamical Detection of Singly-Transiting Circumbinary Planets

MAX GOLDBERG

(Dated: May 2019)

ABSTRACT

Circumbinary planets (CBPs) are exoplanets that orbit completely around a pair of stars. CBPs provide a unique perspective on planet formation and evolution, but the current sample of transiting circumbinary planets is too small to draw conclusions on the population as a whole. Key questions include the distribution of orbital distances compared to the stability limit as well as the coplanarity of circumbinary systems. We searched for transiting circumbinary planets in the catalog of eclipsing binaries from the K2 mission. We found two candidate single-transit events, including one that might show asymmetry in the durations of ingress and egress that could be produced by the acceleration of the star during the transit. We use a simplified photodynamical model that simulates the planet during the transit and constrains its motion. Furthermore, we use eclipse timing variations caused by the apsidal precession of the binary to constrain the mass and orbit of this planet, although a full orbital solution is not possible. Our results suggest there is a possibility to discover and constrain more CBPs by searching in shorter-baseline photometric data from K2 or TESS, which observe more stars than Kepler but for much shorter durations.

1. INTRODUCTION

Approximately half of stars near the Sun are in binary or higher multiplicity systems (Tokovinin 2014). Planets in binary systems can orbit around a single star (s-type, or circumstellar planets) or entirely around the stellar binary. The latter are referred to as p-type, or circumbinary planets (CBPs). Circumbinary planets provide a unique window into planet formation and evolution and represent planetary systems that are distinctly different from our Solar System.

Two parameters are uniquely important in the study of circumbinary systems. Circumbinary planet stability is largely determined by whether the planet is far enough from the host binary that there is no qualitative change to the orbit (e.g. ejection from the system, or collision with a star) over the lifetime of the stars. This inner stability limit is referred to as the *critical semi-major axis*, a_c, and is often given as a function of the binary mass ratio, eccentricity, and semi-major axis (Holman & Wiegert 1999). For example, the Holman-Wiegert stability limit for a test particle around a circular, equal-mass, binary is approximately $a_c = 2.39a_1$, where a_1 is the binary semi-major axis.

The *mutual inclination* i_m is the angle between the orbital planes of the binary and the planet. A planetary orbit with i_m near 0° is referred to as *prograde*, and one with i_m near 180° is *retrograde*. In both cases the orbits are considered *coplanar*. If the orbits of a planet and a binary are mutually inclined, the angular momentum vector of the planet's orbit will precess around the angular momentum vector of the binary's orbit. In particular, the sky plane inclination of the planet will vary and the planet will oscillate between configurations where the planet transits (passes in front of one or both of its stars) and where it does not transit. In fact, planets with more than a slight i_m are almost certain to transit sometime during their precession cycle (Martin & Triaud 2015).

The critical semi-major axis and the mutual inclination are also relevant from the perspective of planet formation. The stability criterion also applies to gas particles in a protoplanetary disk, which truncates the inner part of the disk at approximately a_c. Furthermore, viscous forces within the disk evolve the mutual inclination to 0°, 90°, or 180°, depending on initial conditions (Martin & Lubow 2017). Both effects have been observed around HD 98800B (Kennedy et al. 2019).

To date, the method of exoplanet detection responsible for the majority of detected planets in `exoplanet.eu` (Schneider et al. 2011) has been the transit method. Planets in orbits that are nearly edge-on to the line-of-sight may transit their host star, decreasing its apparent brightness. From continuous photometry of a star with a transiting exoplanet, the planet's orbital period and the ratio of the planet to star radius can be measured. Wide-field broadband photometry surveys such as *Kepler* or *TESS* are especially suited for these detections, as they can simultaneously measure photometry for hundreds of thousands or millions of stars.

Transits of circumbinary planets are unique in two important ways. First, multiple host stars allow for two or more transits during one passage of the planet in front of the binary. Second, the stars themselves are moving, so the transit does not necessarily occur during the same phase of the planet's orbit. As a result, the transits are not necessarily

periodic; rather, they can happen within a range of orbital phases determined by the size of the inner binary. The transit durations can also vary depending on the relative speed of the planet and star.

The quasi-periodicity of CBP transits creates difficulties for transit search algorithms such as Box Least Squares, which generally rely on phase-folding multiple transits at a single period to increase the signal-to-noise ratio. Instead, circumbinary planet transits have been identified by eye, with manual searches of light curves of known eclipsing binary stars (Martin 2018). Nevertheless, a dozen or so circumbinary planets have been discovered, beginning with Kepler-16 (Doyle et al. 2011) and including a three-planet system, Kepler-47 (Orosz et al. 2019). While it is difficult to find transiting CBPs, once a planet is discovered, it can be characterized extensively. The variations in phase, depth, and duration of each transit constrain strongly almost every aspect of the system architecture.

The detections of transiting CBPs have been characterized by an apparent “pile-up" of CBPs near the critical semi-major axis (see Figure 1), as well as a concentration of mutual inclinations near zero. Notwithstanding the small number of detections, statistical analyses of circumbinary systems have asked whether these trends in CBP detections are statistically significant, and to what extent they are affected by detection biases (Li et al. 2016; Quarles et al. 2018). The conclusions of these studies have varied, but a consensus is that a larger sample will be required to make statistically significant claims.

We searched for additional CBP candidate signals in a newer photometry data set, K2, to attempt to increase the CBP sample.

2. PHOTOMETRIC DATA

Kepler was a space telescope that observed a $\sim$100 deg^2 field of the sky at high photometric precision continuously for about 4 years, but the failure of two reaction wheels necessitated a redesign of the mission. The new mission, K2, used the same telescope to observe $\sim$ 100 deg^2 fields along the ecliptic for 19 “Campaigns" each lasting approximately 70 days, from March 2014 to July 2018. Some campaigns overlapped in footprint, so that observation baselines for particular targets exceeded a year in some cases.

The lack of precise pointing on the satellite results in significant data artifacts that must be corrected to detect planetary transits. We used EVEREST (Luger et al. 2018) to detrend light curves, selecting a custom aperture that minimized scatter. EVEREST uses a Pixel Level Deconvolution model that necessitates masking large variations such as eclipses and transits. We included these masks for the two candidate signals discussed below.

3. ECLIPSING BINARY SAMPLE

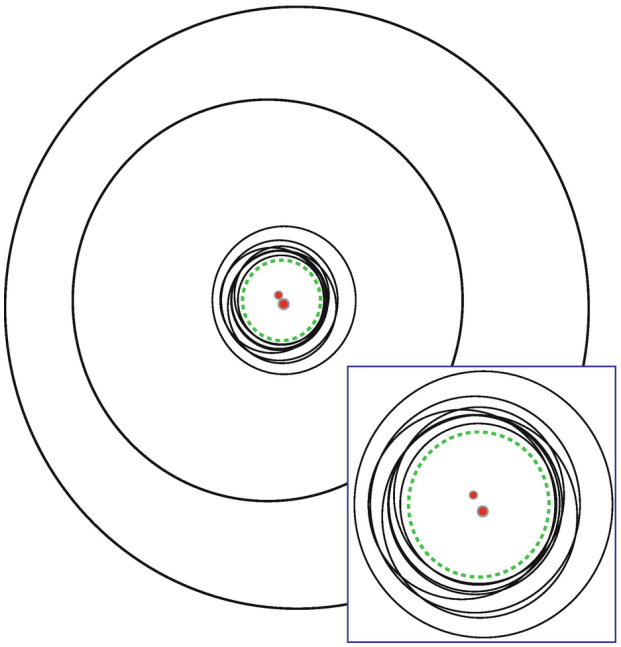

Figure 1. The orbits of the first 10 discovered *Kepler* circumbinary planets, scaled to their critical semi-major axis (shown as the green dashed circle). The inset is a zoom of the planets near the stability limit. The outermost orbit is Kepler-1647b, the next one is Kepler-47c. The stars are illustrative and not to scale. (figure credit: Welsh & Orosz (2018))

For our sample, we considered all targets identified as eclipsing binaries in the Kepler Eclipsing Binary Catalog (Prša et al. 2011) with periods greater than 5 days. We selected this constraint primarily because no transiting planets have been found around eclipsing binaries with periods below 5 days. Additionally, the rapidly varying velocities of the stars may change the transit shape enough to make it unrecognizable.

178 objects in this sample have measured binary periods between 5.001d and 54.2d with a median period of 10.7d. Ten additional objects have unmeasured periods because no repeated eclipses were detected.

Planetary transits are often dwarfed by larger-amplitude variations in the light curve from starspots, and in these cases, stellar eclipses. We found that a flat out-of-eclipse flux was ideal for searching for shallow transits by eye, and therefore we adopted a method based on Gaussian processes to remove fluctuations from spots. We determined that the Gaussian process kernel described in Angus et al. (2018) fit to the out-of-eclipse flux data removed the stellar variations effectively. A Gaussian process kernel can be uniquely defined by the matrix of covariance of the data with itself, $k_{i,j}$. This matrix has dimension $N \times N$, where N is the number of data points. This kernel has 5 parameters, and its covariance takes the form

$$k_{i,j} = A \exp\left[-\frac{(t_i - t_j)^2}{2l^2} - \Gamma^2 \sin^2\left(\frac{\pi(t_i - t_j)}{P}\right)\right] + \sigma^2 \delta_{ij}$$

where t_i is the i-th time in the light curve.

The approximate physical interpretation of the parameters is that A is the amplitude of auto-correlation with a decay time l, Γ is the amplitude of auto-correlation at the stellar rotation period P, and σ is an intrinsic scatter to help with underestimated uncertainties. Although this model was designed for single stars, we found it remained successful for binary stars with starspots. Such success would be anticipated if the stars have equal spin periods due to tidal locking, or if the spot variations from one star dominate the total flux oscillations.

Once the best-fitting kernel parameters were found for each light curve, we subtracted the kernel's prediction from the overall light curve to obtain a detrended flux where planetary transits are most apparent. An example of this is given in Figure 2, where the extra dip is readily apparent in the fully-detrended light curve.

4. PHOTOMETRIC RESULTS

Two candidate transit signals were found in the searched K2 light curves. One was seen in the Campaign 0 light curve of EPIC 202086627 ($P = 7.1512571$d) near $t = 1955.8$, shortly after a secondary eclipse. Although the star is relatively bright ($Kp = 11.7$), the signal has a depth of only $\sim 0.1\%$, shows little structure, and appears nowhere else in the light curve.

Another candidate transit signal was seen in the Campaign 5 light curve of the eclipsing binary EPIC 211309989 ($P = 7.538515$d, $Kp = 13.9$) near $t = 2360.9$, shortly before a secondary eclipse. If interpreted as a transit, the signal has an approximate depth of 1.4% and duration of 8 hours. EPIC 211309989 was also observed during Campaign 18 (see Figure 6, but no comparable transit events were observed.

We chose to focus on characterizing the signal in EPIC 211309989 because its depth and width were most suggestive of a circumbinary planet. Further, if the deeper signal is indicative of a more massive planet, the prospects for detecting the planet from its gravitational effect on the host binary are better. Therefore, the rest of this work concerns only the signal in EPIC 211309989. A similar analysis, however, could be conducted for EPIC 202086627.

To characterize the orbit of the stellar binary in EPIC 211309989, we used the analytical eclipse model `occultnl` from Mandel & Agol (2002), fitting for orbital parameters and relative radii and fluxes of the stars. Quadratic limb darkening parameters were fixed to $u_1 = 0.38222405$ and $u_2 = 0.33739597$ for both stars. Without radial velocity data, only the eccentricity e_1, the argument of periastron ω_1, the inclination i_1, the relative semi-major axis $a_1/(R_A + R_B)$, the radius ratio R_B/R_A, and the flux ratio $L_A/(L_A + L_B)$ can be measured. We used Levenberg-Marquardt minimization to compute intermediate quantities of the light curve, including the impact parameters and durations of the primary and

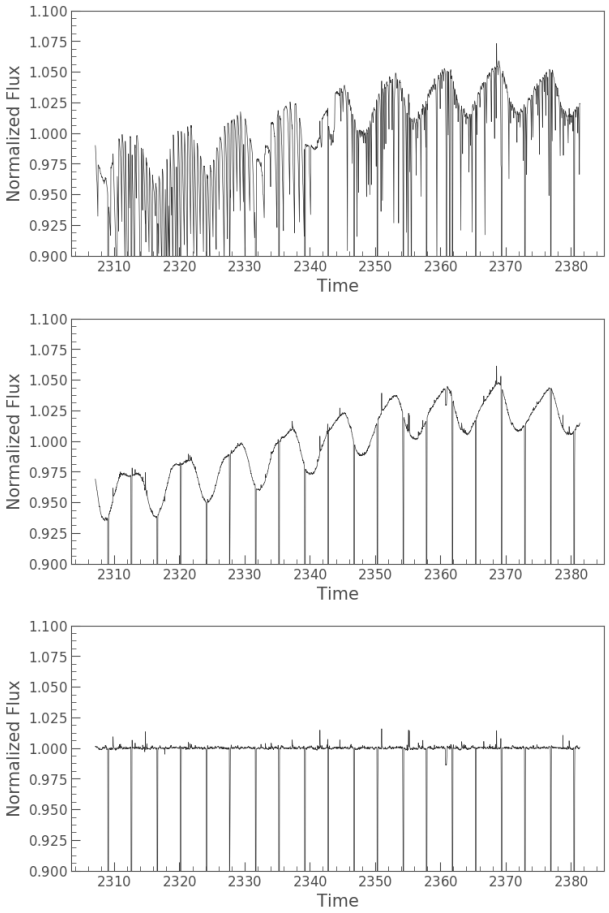

Figure 2. Light curves of EPIC 211309989 from K2 Campaign 5. Top: The raw K2 light curve, derived from Simple Aperture Photometry (SAP) of the K2 postage stamp. Middle: The EVEREST-detrended lightcurve. Bottom: the light curve after removing quasi-periodic stellar variations with a Gaussian process.

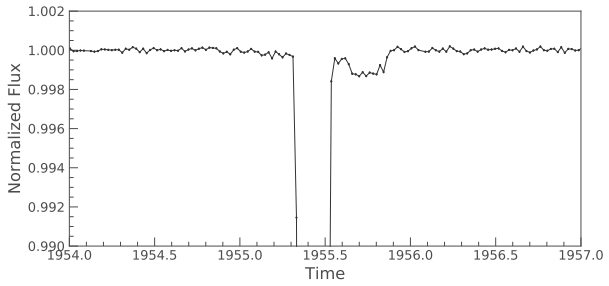

Figure 3. The candidate signal in EPIC 202086627. Error bars represent 1σ photometric uncertainties. The large dip to the left is a secondary eclipse.

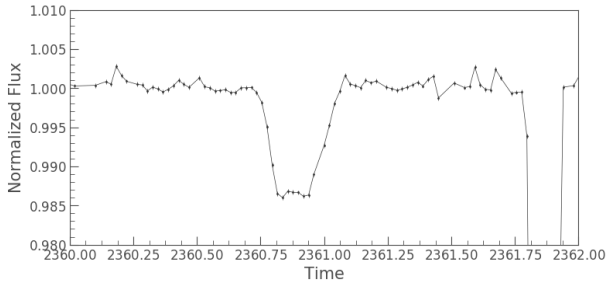

Figure 4. The candidate signal in EPIC 211309989. Error bars represent 1σ photometric uncertainties. The large dip to the right is a secondary eclipse.

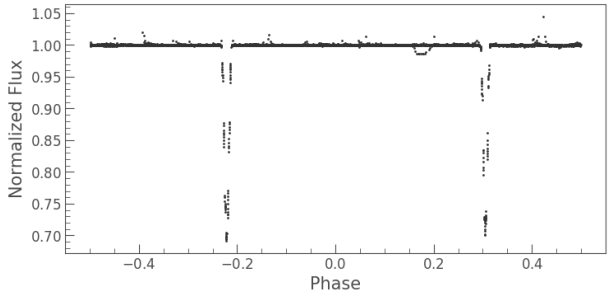

Figure 5. The light curve of EPIC 211309989 detrended with EVEREST and a Gaussian process to remove spot modulations, phase folded at the period of the inner binary. The extra dip appears to be unrelated to the binary period.

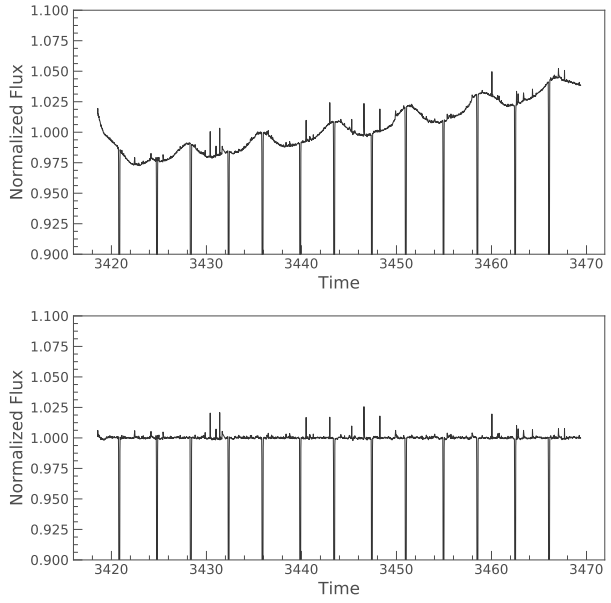

Figure 6. Light curves of EPIC 211309989 from K2 Campaign 18. Top: The EVEREST-detrended lightcurve. Bottom: the light curve after removing quasi-periodic stellar variations with a Gaussian process.

secondary eclipses. We then used the Ensemble Sampler in `emcee` to compute the physical orbital parameters to account for complex correlations between the orbital elements, in particular the pairs e_1, ω_1 and a_1, i_1. The results of the fit are given in Table 1. The binary is slightly eccentric, as expected for its orbital period. Notably, the stars have almost identical radii and fluxes (and hence effective temperatures). The mid-time of eclipses were fit as individual parameters to be used in an eclipse timing analysis described below.

Table 1. The results of the fit to the eclipsing binary model.

Parameter	Mean Value	Uncertainty	Unit
$e_1 \cos\omega_1$	-0.041991	0.000048	
$e_1 \sin\omega_2$	-0.0548	0.0015	
e_1	0.0690	0.0012	
ω_1	-127.46	0.75	degrees
i_1	88.784	0.052	degrees
$a_1/(R_A+R_B)$	15.398	0.074	
R_B/R_A	1.00	0.16	
$L_A/(L_A+L_B)$	0.52	0.10	

A rough mass constraint on the stars was useful for simulating orbital dynamics. We fit SDSS, Gaia, and 2MASS photometric fluxes to MIST stellar models in the `isochrones` package. Because the stars appear to be identical within measurement uncertainties, we considered the system to be a single star and inflated the parallax by a factor of $\sqrt{2}$. The derived stellar mass and radius were approximately $0.6 M_\odot$ and $0.55 R_\odot$, respectively. As the luminosity and radius of the stars were found to be consistent with each other, within measurement uncertainties, and the age and metallicity are assumed to be the same because the stars likely formed from the same gas cloud, we adopt these mass and radius values for both stars.

5. PHOTODYNAMICAL TRANSIT MODEL

The transit candidate in Figure 4 appears to show asymmetry in that the durations of ingress and egress differ by a factor of ~ 2. For non-grazing transits without limb darkening, the duration of ingress or egress is

$$\tau = \frac{r_p}{v_r \sqrt{1-b^2}},$$

where v_r is the relative speed between the planet and star and b is the (instantaneous) impact parameter. Such an asymmetry, therefore, could be produced by a difference in relative speed during ingress and egress, or a different instantaneous impact parameter. Both phenomena could occur due to the acceleration of the star being transited, and would be a re-

markable confirmation that the dip signal is actually a body transiting the binary.

What additional information does the asymmetry provide? Consider a planet transiting a star with x-y plane velocity $\mathbf{v_r}$ relative to the star, and take the star to have constant x-y plane acceleration $\mathbf{a}$. For simplicity, assume also that the impact parameter of the transit does not vary over the transit duration T, and that $|\mathbf{a}T| \ll |\mathbf{v_r}|$. Then, the ratio of ingress to egress duration is

$$\frac{\tau_i}{\tau_e} = \frac{|\mathbf{v_r}|}{|\mathbf{v_r}+\mathbf{a}T|} \approx \frac{|\mathbf{v_r}|}{\sqrt{|\mathbf{v_r}|^2+2\mathbf{v_r}\cdot\mathbf{a}T}} \approx 1-\frac{\mathbf{v_r}\cdot\mathbf{a}T}{|\mathbf{v_r}|^2}.$$

Hence, the ingress/egress asymmetry constrains the angle between the planet's motion and the acceleration of the star behind it.

To quantify this more precisely, we constructed a partial photodynamical model of the system. We created a two-body system of the binary according to the parameters in Table 1, and then simulated the planet as moving at a constant velocity in front of the stars. The sky-plane is the x-y plane, and the observed lies on the positive z-axis. At every K2 cadence between t = 2360.6 BKJD and t = 2361.2 BKJD, we used the analytical occultation model from Mandel & Agol (2002) to compute the system flux. Quadratic limb darkening parameters of $u_1 = 0.2459$, $u_2 = 0.4397$, appropriate for a $T_{eff} = 3650K$, $\log g = 4.75$, [Fe/H]=-0.5, star were interpolated from the stellar photosphere simulations in Claret & Bloemen (2011).

Seven parameters were fit in the model. Four represented the motion of the planet: the position (x_0, y_0) of the planet relative to the transited star at the approximate transit mid-time t = 2360.89 BKJD, and the planet velocity components v_x and v_y relative to the binary center-of-mass. Additional parameters were the planet-to-star radius ratio r_p/R_s, the out-of-transit flux f_0, and an intrinsic scatter σ, which was used because stellar variability exceed the photometric uncertainty. We used the Ensemble Sampler in `emcee` to sample the posterior distributions of these parameters. A simulated light curve of the best-fitting model is shown in Figure 7.

Four constraints on the planet position and velocity are insufficient to derive a six-parameter Keplerian orbital solution. Assuming the planet's orbit is circular reduces the number of parameters to four and enables a solution, so we do that here to derive orbital elements. Small orbital eccentricities, which are seen in the discovered CBP population (Li et al. 2016), would slightly modify the following quantities. Note that all of the following orbital elements are defined with respect to the binary center-of-mass. As the transit occurs with a small projected distance to the binary center-of-mass, the planet has only a small radial velocity at the time of the transit. Therefore, the planet semi-major axis can be computed

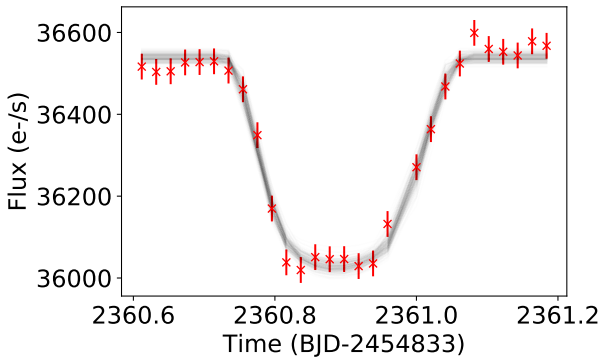

Figure 7. The best-fitting photodynamical model for a planet transiting the primary star. Red points are detrended K2 fluxes (equivalent to Figure 4), with error bars representing the mean scatter from the fit. Gray lines are flux models produced from 200 samples from the posterior.

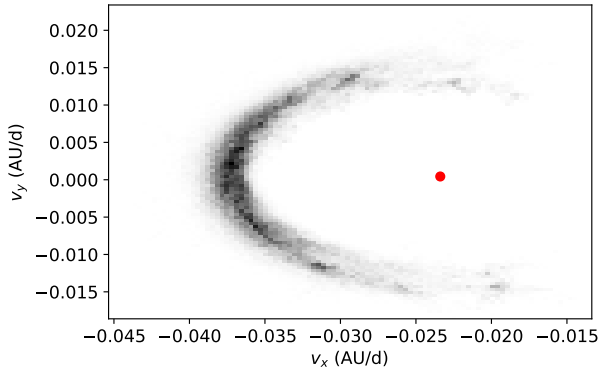

Figure 8. The posterior of the planet's velocity components v_x and v_y, when the planet transits the primary star. The single red point is the velocity of the primary star at the transit mid-time.

from $v = \sqrt{v_x^2+v_y^2}$ with

$$a_b = \frac{GM_{AB}}{v^2} \tag{1}$$

and likewise the period with

$$P_b = \frac{2\pi GM_{AB}}{v^3} \tag{2}$$

where M_{AB} is the total binary mass and G is the Newtonian gravitational constant.

Furthermore, the relative longitude of the ascending node is

$$\Delta\Omega = \mathrm{atan2}(v_y, v_x)+\pi \tag{3}$$

and the planet sky-plane inclination is

$$i_2 = \frac{\pi}{2} - \sin^{-1}\frac{|v_x y_p - v_y x_p|}{v a_b} \tag{4}$$

where atan2 is the two-argument arctangent function, and (x_p, y_p) is the position of the planet at any time, relative to the binary center-of-mass. Note that i_2 will be close to 90° by virtue of the existence of a planet transit, with a lower limit set by the projected distance of the star from the binary center-of-mass.

As a function of these observable angles, the mutual inclination is

$$i_m = \cos^{-1}(\cos i_1 \cos i_2 + \sin i_1 \sin i_2 \cos \Delta\Omega) \quad (5)$$

where i_1 is the binary sky-plane inclination.

It is not clear *a priori* which star is being transited. Therefore, we computed posterior distributions of the seven parameters for both cases.

6. MODELING RESULTS

The relative size of the planet is well-constrained to be $r_p/R_A = 0.1652 \pm 0.0048$, or $r_p/R_B = 0.1649 \pm 0.0049$. With $R_A = R_B = 0.55 R_\odot$, this corresponds to $r_p \approx 0.9 R_J$.

The transit shape and duration constrain the relative motion of the planet across the star. The impact parameter at t = 2361.89 BKJD is 0.732 ± 0.058, and the relative speed of the planet is well-constrained to 0.0142 ± 0.0013 AU/d. However, the direction of this motion is poorly constrained (Figure 8), which leads to large uncertainty in the planet's motion relative to the system center-of-mass and therefore in the derived planet period (Figure 12).

Aligned orbits lead to periods as short as 60 days. Such orbits appear to be stable, as the stability limit is at an outer orbital period of $\sim$ 30d. However, the period and mutual inclination are strongly correlated, see Figure 11. Transits across the primary star lead to prograde orbits, while those across the secondary star are retrograde. This is expected, because the planet must nearly match the speed of the stars to generate a transit that lasts longer than the eclipses.

The transit is near-grazing, as seen in Figure 9.

7. ECLIPSE TIMING ANALYSIS

If a stellar binary has an outer third body, it will perturb the inner orbits from pure Keplerian ellipses. This can be detected in photometry if the perturbations change the timing of the stellar eclipses. The actual form of these perturbations is complicated; see Borkovits et al. (2015) for discussions of these effects. The high-precision photometry provided by Kepler and K2 allows for extremely high-precision measurements of eclipse mid-times, in many cases approaching the $\sim$ 1s level for long-cadence (30 minute) photometry. For example, if a $1 M_J$ planet were in an 80d circular and coplanar orbit around EPIC 211309989, n-body simulations predict it would cause eclipse timing variations on the order of 5s at the period of the planet. Such a dynamical detection could therefore be plausible.

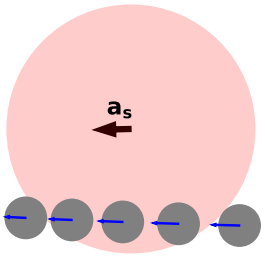

Figure 9. The path of the planet during the best fit transit across the primary star. The path is not straight due to the acceleration of the star during the transit. Blue arrows represent the instantaneous velocity of the planet, the black arrow shows the acceleration of the star, responsible for the changing velocity of the planet.

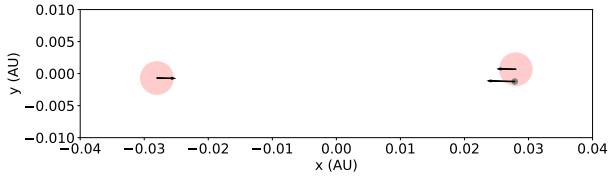

Figure 10. A cartoon of the best-fitting primary-transiting system, at the time of mid-transit. Black arrows represent the velocity of the stars and the planet, and are to scale.

However, the eclipse mid-times have a significant systematic uncertainty due the presence of starspots. If one star crosses a spot on the other star not directly in the line of sight, the eclipse profile becomes asymmetric and the fitted eclipse mid-time shifts (Orosz et al. 2012). The variation in the out-of-eclipse flux visible in the middle panel of Figure 2 is indicative of starspots capable of causing these offsets. One solution for correcting the eclipse times is to fit a linear relationship between the deviation of the eclipse time from a linear ephemeris with the local slope of the light curve around the eclipse (Orosz et al. 2012). Unfortunately, EPIC 211309989 is probably an unsuitable candidate for this analysis because the total number of eclipses is small, and the nearly-equal-brightness stars makes it difficult to determine on which star the spots lie.

Eclipse timing variations due to the secular precession of the periastron of the inner binary, however, may be measurable, and less susceptible to offsets from starspots because only long-term trends are relevant. When the argument of periastron, ω_1, varies, the orbital ellipses do not perfectly close, leading to slightly different periods of primary and secondary eclipses.

The difference between the periods measured solely by primary eclipses and solely by secondary eclipses is given by

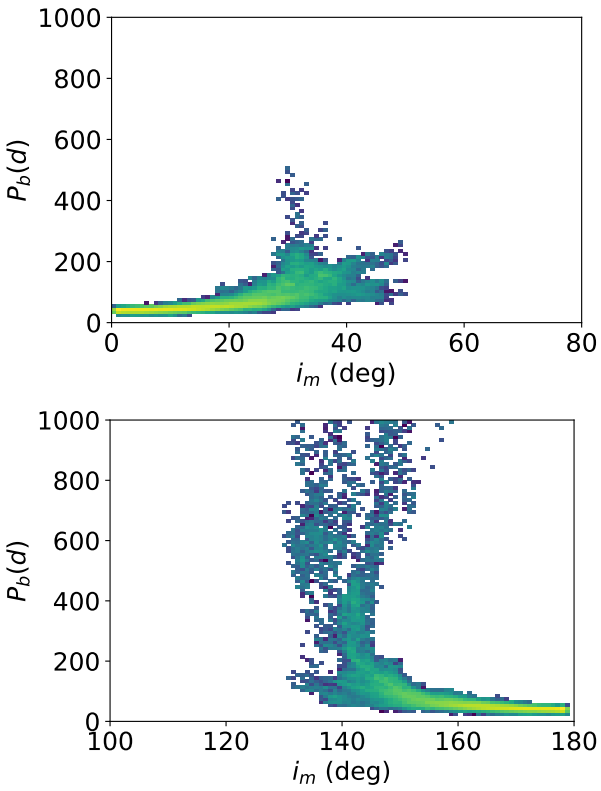

Figure 11. The correlation between the derived planet period and mutual inclination of the transiting object. The top panel is for transits of the primary star, the bottom panel is for the secondary star.

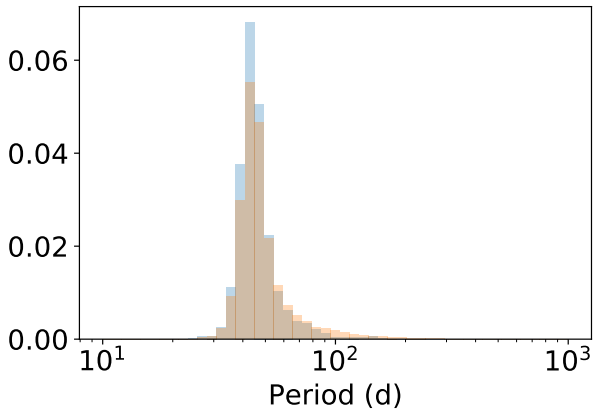

Figure 12. The posterior distribution of the planet's period, depending on which star is being transited.

(Zhang & Fabrycky 2019)

$$P_A - P_B = \frac{2e_1 \sin\omega_1 (1-e_1^2)^{\frac{3}{2}}}{\pi(1-e_1^2\sin^2\omega_1)^2} P_1^2 \dot{\omega}. \quad (6)$$

Mechanisms other than a third body can drive periastron precession, in particular, relativistic effects and tides raised on the stars by each other. An overview is in Zhang & Fabrycky (2019), but the relevant formulae are repeated here:

The first-order relativistic correction is

$$\dot{\omega}_{GR} = \frac{3G^{3/2}M_{AB}^{3/2}}{a_1^{5/2}c^2(1-e_1^2)} \quad (7)$$

where M_{AB} is the binary mass and c is the speed of light.

The precession due to tides raised on the stellar surfaces is

$$\dot{\omega}_T = 30\pi \frac{G^{1/2}M_{AB}^{1/2}}{a_1^{13/2}} \frac{1+(3/2)e_1^2+(1/8)e_1^4}{(1-e_1^2)^5} \times \left(\frac{M_B}{M_A}k_{2A}R_A^5 + \frac{M_A}{M_B}k_{2B}R_B^5\right) \quad (8)$$

where k_{2A} and k_{2B} are the Love numbers of the primary and secondary stars, and R_A and R_B are the stellar radii.

The contribution from the quadrupole moment of a coplanar orbiting third-body is

$$\dot{\omega}_{3b} = \frac{G^{1/2}m_b a_1^{3/2}}{M_{AB}^{1/2}a_b^3}\frac{3}{4}(1-e_1^2)^{1/2} \quad (9)$$

where m_c is the third-body mass and a_2 is its semi-major axis. Small contributions to $\dot{\omega}$ can be added linearly.

The primary and secondary eclipse mid-times from Campaigns 5 and 18 are shown in Table 2 and Figure 13, along with the raw 1σ uncertainties. A linear fit to every eclipse time determines $P_A - P_B = -0.23 \pm 0.11$s. Using equation 6, this corresponds to $\dot{\omega} = 0.029 \pm 0.014$ deg/yr, a weak detection of precession but a useful upper limit.

The relativistic correction can be explicitly calculated, and we find $\dot{\omega}_{GR} = 0.0078$ deg/yr. Taking $k_{2A} = k_{2B} = 0.07$ for a $0.6M_\odot$, 7Gyr old star (Claret 1997), we calculate $\dot{\omega}_T = 0.0123$ deg/yr. The remaining precession, $\dot{\omega}_{3b} = 0.009 \pm 0.014$ deg/yr, we assign to third-body motion, although it is consistent with zero. Converted to a third-body mass and period constraint, we find $m_c/P_b^2 = 0.043 \pm 0.070 M_J/\mathrm{yr}^2$. This lack of excess precession places a strong upper limit on the mass of a third-body.

Close orbits, under 400 days, are likely ruled out as the transit depth is indicative of a Jupiter-radius body, which has a physical lower limit on mass (Figure 14). The indicated allowed periods, above 400 days, are in conflict with the periods determined from partial photodynamical modeling (Figure 12). Possible resolutions to this disagreement, from most mild to most dramatic, are (a) that the planet's orbit is actually eccentric and the transit is near periastron, (b) we over-interpreted the asymmetry signal and the planet transited on a slower orbit, or (c) the transit is due to a background system or instrumental artifact and does not indicate a CBP at all.

8. CONCLUSION

We have reported on a candidate transit signal in the light curve of the eclipsing binary EPIC 211309989. An apparent

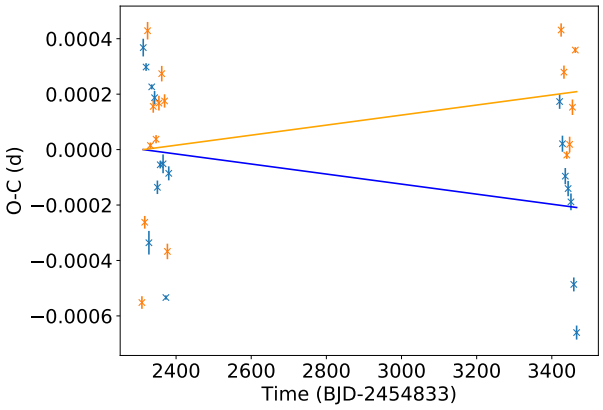

Figure 13. Eclipse timing variations of EPIC 211309989. Blue points are primary eclipses, orange are secondary. Error bars represent raw 1σ uncertainties. The blue and orange lines are linear fits to the ETVs, representing an offset in period between the primary and secondary eclipses.

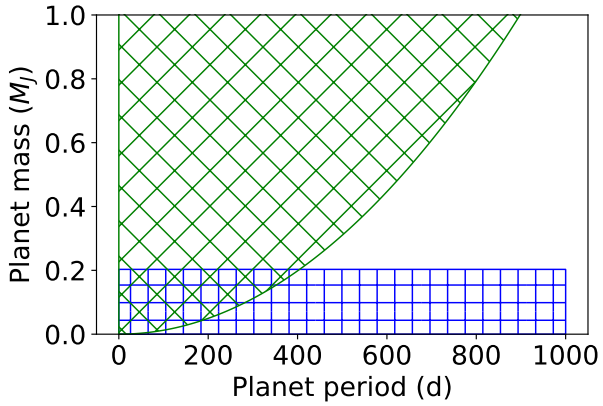

Figure 14. Combined constraints of radius from transit depth and mass from apsidal precession. Blue hatches are planet masses ruled out at 95% confidence assuming a $0.9R_J$ planet and intrinsic scatter in the mass-radius relation from Chen & Kipping (2017). Green hatches are ruled out at 95% confidence from the apsidal precession attributed to the planet.

asymmetry in the signal due to the acceleration of the stars constrains the motion of the planet and hence an orbital period.

Eclipse timing from K2 photometry constrains the orbit of the third body, ruling out closely orbiting gas giants. A distant, puffy planet is roughly consistent with the observed transit and eclipse times, but its orbital parameters are underconstrained with available data. Follow-up radial velocity observations could better characterize the binary or directly detect the planet. Additional observations of eclipses would also be useful to extend the timing baseline and precisely measure the apsidal precession rate. And, a full analysis of starspots could improve both the transit and eclipse fits and determine whether the transit asymmetry is due to dynamics, starspots, or instrumental artifacts. Finally, if this is a bona-fide planet in a circumbinary orbit, it will transit again in the future, although the exact time cannot be predicted.

My greatest thanks is to my thesis advisor Daniel Fabrycky, who guided this project from start to finish and improved it every step of the way. I have benefited enormously from two years of research and conversations with him about exoplanets and astrophysics, and his boundless curiosity has continuously inspired and encouraged me.

Throughout this project, I have been very fortunate to have had discussions with Ben Montet, David Martin, and Andrew Vanderburg, whose deep knowledge of K2 data and possible signals has been invaluable. I am especially grateful to my thesis readers, Dorian Abbot and Leslie Rogers, who provided excellent advice and critiques that were crucial in bringing this work to its current state. Additionally, I am indebted to the Department of Astronomy & Astrophysics, not only for the education they provided me, but also for the chance to earn a degree and write a thesis in Astronomy & Astrophysics. In particular, Julia Borst Brazas, Rich Kron, and John Carlstrom were endlessly determined to make this a reality.

Finally, I am thankful for the support of the the first class of Astronomy & Astrophysics Majors at the University of Chicago. We all decided to switch because of a love of astronomy, and this commitment shone through as we navigated and shaped the new major.

REFERENCES

Angus, R., Morton, T., Aigrain, S., Foreman-Mackey, D., & Rajpaul, V. 2018, MNRAS, 474, 2094

Borkovits, T., Rappaport, S., Hajdu, T., & Sztakovics, J. 2015, MNRAS, 448, 946

Chen, J., & Kipping, D. 2017, ApJ, 834, 17

Claret, A. 1997, VizieR Online Data Catalog, J/A+AS/125/439

Claret, A., & Bloemen, S. 2011, A&A, 529, A75

Doyle, L. R., Carter, J. A., Fabrycky, D. C., et al. 2011, Science, 333, 1602

Holman, M. J., & Wiegert, P. A. 1999, AJ, 117, 621

Kennedy, G. M., Matrà, L., Facchini, S., et al. 2019, Nature Astronomy, 3, 230

Li, G., Holman, M. J., & Tao, M. 2016, ApJ, 831, 96

Luger, R., Kruse, E., Foreman-Mackey, D., Agol, E., & Saunders, N. 2018, AJ, 156, 99

Mandel, K., & Agol, E. 2002, ApJL, 580, L171

Martin, D. V. 2018, Populations of Planets in Multiple Star Systems, 156

Martin, D. V., & Triaud, A. H. M. J. 2015, MNRAS, 449, 781

Martin, R. G., & Lubow, S. H. 2017, ApJ, 835, L28

Orosz, J. A., Welsh, W. F., Carter, J. A., et al. 2012, Science, 337, 1511

Orosz, J. A., Welsh, W. F., Haghighipour, N., et al. 2019, AJ, 157, 174

Prša, A., Batalha, N., Slawson, R. W., et al. 2011, AJ, 141, 83

Quarles, B., Satyal, S., Kostov, V., Kaib, N., & Haghighipour, N. 2018, ApJ, 856, 150

Schneider, J., Dedieu, C., Le Sidaner, P., Savalle, R., & Zolotukhin, I. 2011, A&A, 532, A79

Tokovinin, A. 2014, AJ, 147, 87

Welsh, W. F., & Orosz, J. A. 2018, Two Suns in the Sky: The Kepler Circumbinary Planets, 34

Zhang, Z., & Fabrycky, D. C. 2019, arXiv e-prints, arXiv:1905.10179

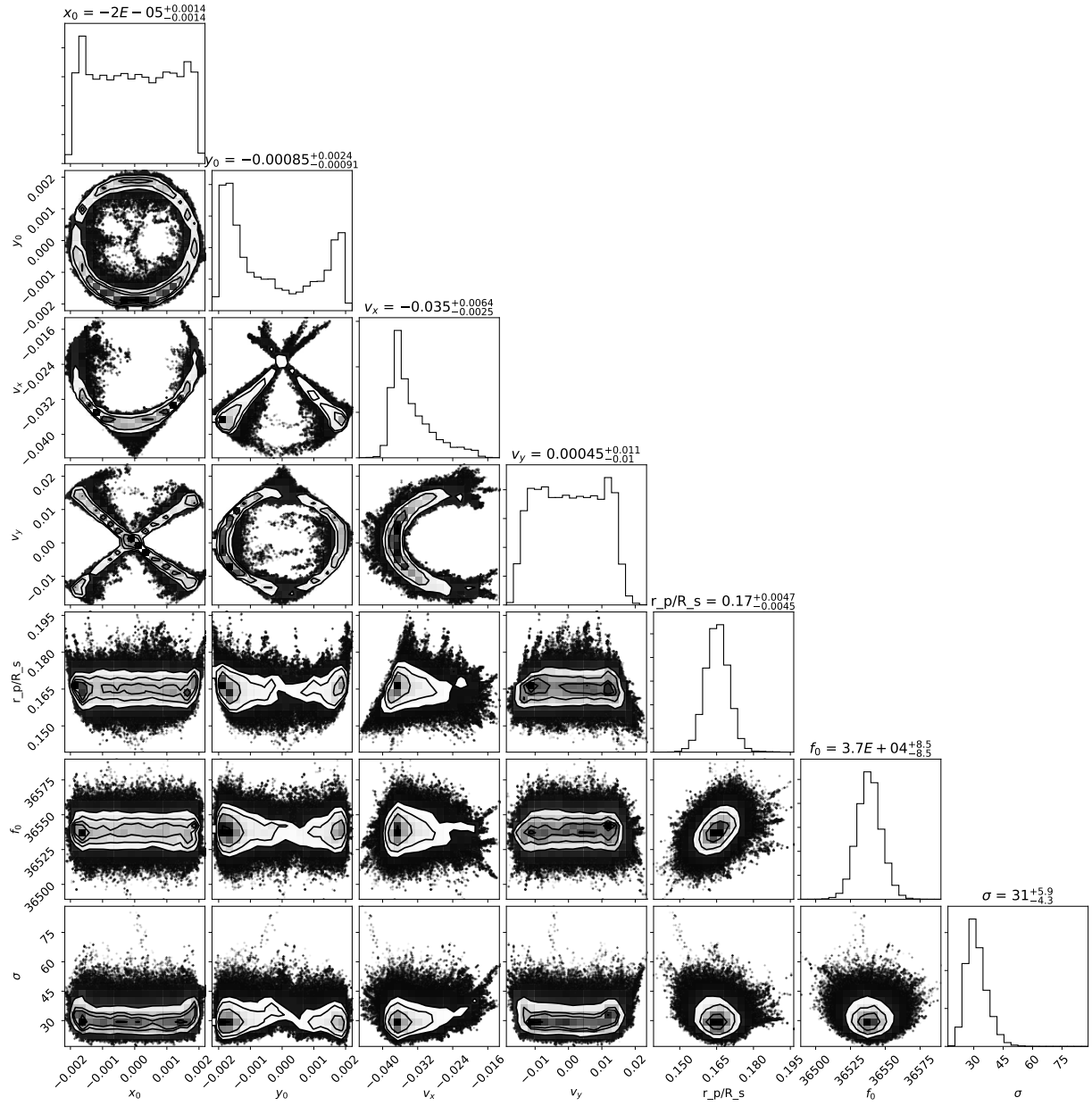

Figure 15. The correlations between the seven parameters in the transit fit, assuming the planet transits the primary star. Units are AU for x_0, y_0, AU/d for v_x, v_y, and e-/s for f_0 and σ.

Table 2. The eclipse mid-times in BKJD (BJD-2454833) from the light curve fit. Integer indices represent primary eclipses, while half-integer indices represent secondary eclipses.

Eclipse index	Eclipse time	Uncertainty	Eclipse index	Eclipse time	Uncertainty
1	2312.662516	0.000032	0.5	2309.094480	0.000023
2	2320.200961	0.000014	1.5	2316.633284	0.000023
3	2327.738842	0.000043	2.5	2324.172490	0.000032
4	2335.277920	0.000009	3.5	2331.710592	0.000010
5	2342.816396	0.000024	4.5	2339.249248	0.000023
6	2350.354588	0.000024	5.5	2346.787644	0.000015
7	2357.893184	0.000013	6.5	2354.326290	0.000027
8	2365.431703	0.000034	7.5	2361.864911	0.000028
9	2372.969735	0.000008	8.5	2369.403328	0.000024
10	2380.508698	0.000025	9.5	2376.941300	0.000028
148	3420.824038	0.000026			
149	3428.362400	0.000029	148.5	3424.795694	0.000024
150	3435.900799	0.000029	149.5	3432.334057	0.000024
151	3443.439269	0.000028	150.5	3439.872273	0.000014
152	3450.977736	0.000030	151.5	3447.410826	0.000028
153	3458.515953	0.000025	152.5	3454.949476	0.000028
154	3466.054295	0.000025	153.5	3462.488197	0.000010